Supporting Information

Oxygen Evolution Reaction Dynamics, Faradaic Charge Efficiency, and the Active Metal Redox States of Ni-Fe Oxide Water Splitting Electrocatalysts

Mikaela Görlin[1], Petko Chernev[2], Jorge Ferreira de Araújo[1], Tobias Reier[1], Sören Dresp[1], Benjamin Paul[1], Ralph Krähnert[1], Holger Dau[2], and Peter Strasser[1]

[1] Technical University of Berlin, Chemical Engineering, Straße des 17. Juni 124, 10623, Berlin, Germany
[2] Free University of Berlin, Department of Physics, Arnimallee 14, 14195 Berlin, Germany

Contacts:
pstrasser@tu-berlin.de
holger.dau@fu-berlin.de

S1. Electrochemical characterization

S1.1. OER activity

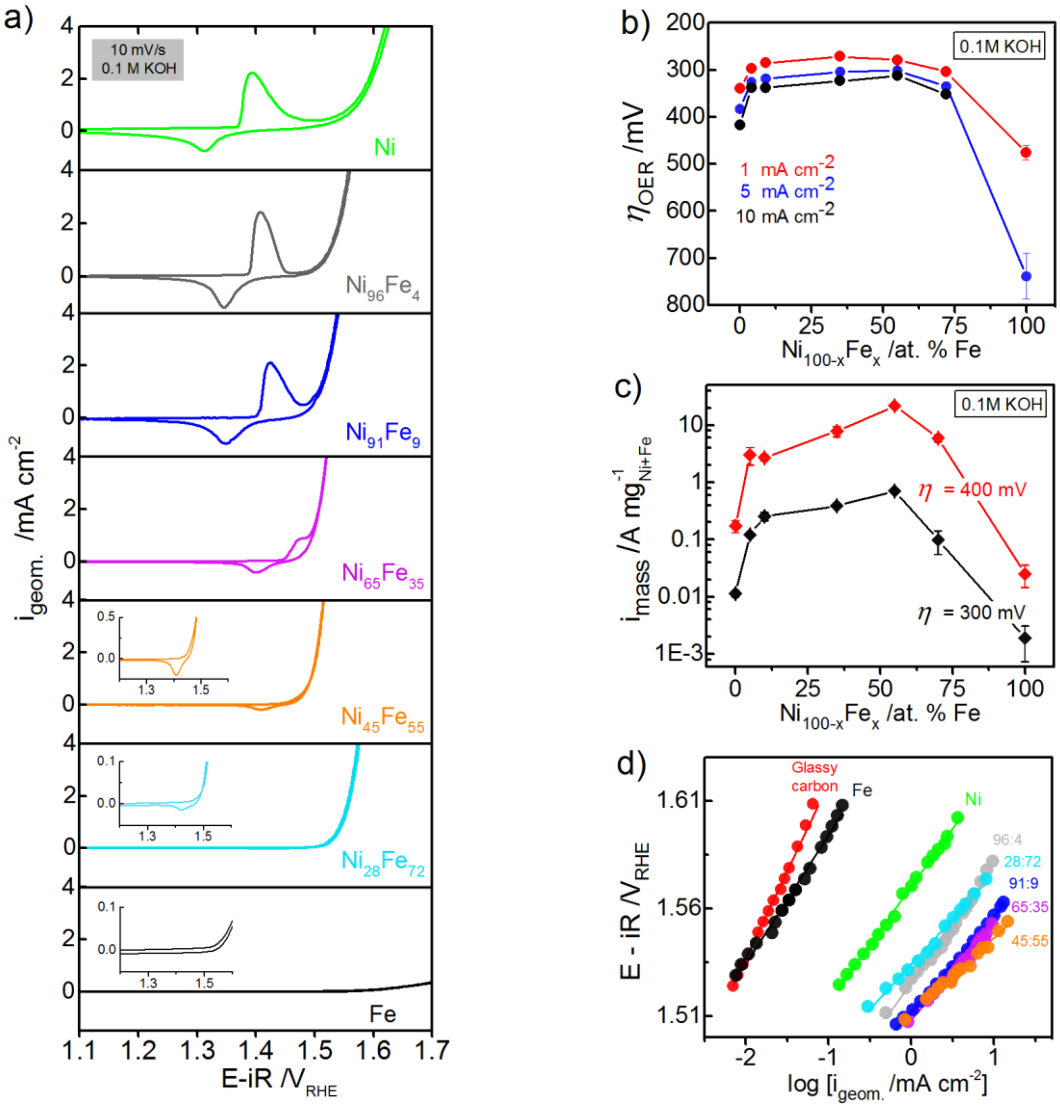

Figure S1. **(a)** CVs measured at 10 mV/s in rotating disk electrode (RDE) setup after an initial pre-conditioning step of 1.63 V_{RHE} for 30 min in 0.1 M KOH. **(b)** Overpotential (η_{OER}) at 1, 5, and 10 mA cm^{-2}, extracted from chronopotentiometric measurements. **(c)** Mass activity (i_{mass}) based on the total metal loading obtained by ICP-OES. **(d)** Tafel plots obtained from quasi-stationary state measurements by applying a stable potential for 90 s in 0.1 M KOH. The catalyst composition, $Ni_{100-x}Fe_x$, is indicated as atomic %. The total geometric metal loading was determined by ICP-OES prior to the measurements, kept at ~10 µg Ni+Fe cm^{-2} in the presented measurements. The rotation speed was set to 1600 rpm.

S1.2. The effect of applying reducing potential

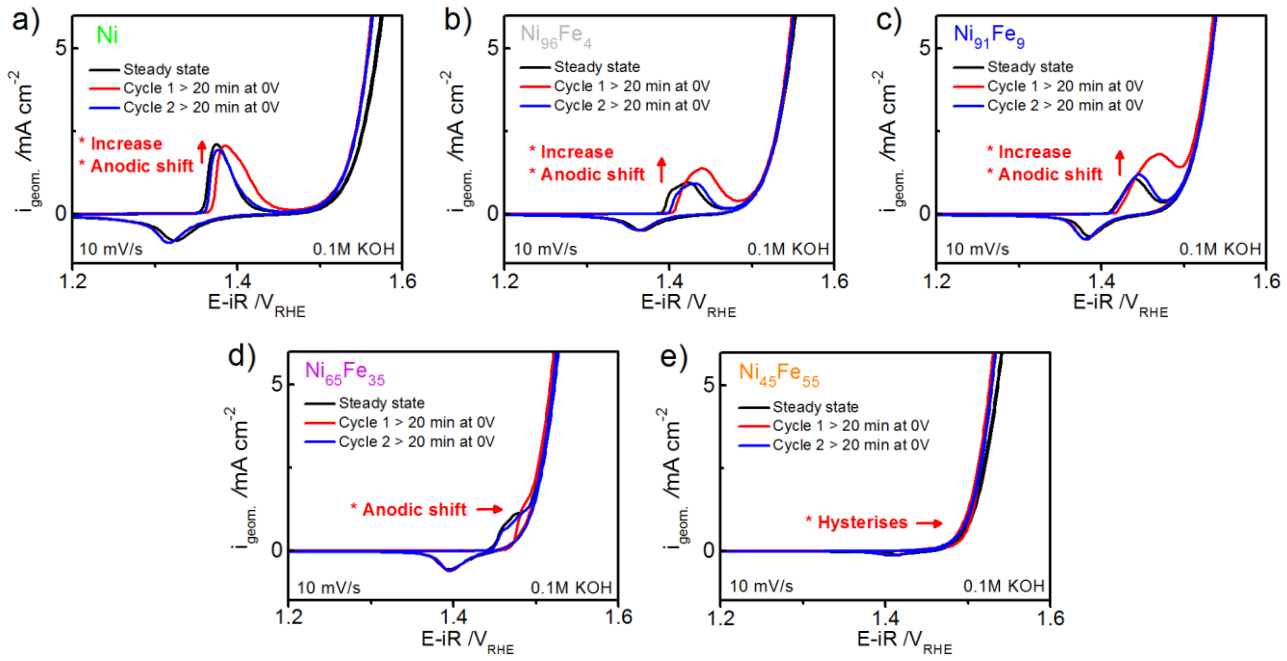

Figure S2. CVs measured before and after application of a reducing potential (0 V_{RHE}) for 20 min to make sure all Ni centers were in the reduced state, according to the principle presented by Batchellor et al [1]. **(a)** The Ni catalyst **(b)** $Ni_{96}Fe_4$ **(c)** $Ni_{91}Fe_9$ **(d)** $Ni_{65}Fe_{35}$ **(e)** $Ni_{45}Fe_{55}$. CVs were recorded in RDE setup at a scan-rate of 10 mV/s, a rotation speed of 1600 rpm, and a metal loading of ~ 6 µg Ni+Fe cm^{-2}. The catalyst composition ($Ni_{100-x}Fe_x$) is given as atomic %.

S1.3. Conditioning of catalysts

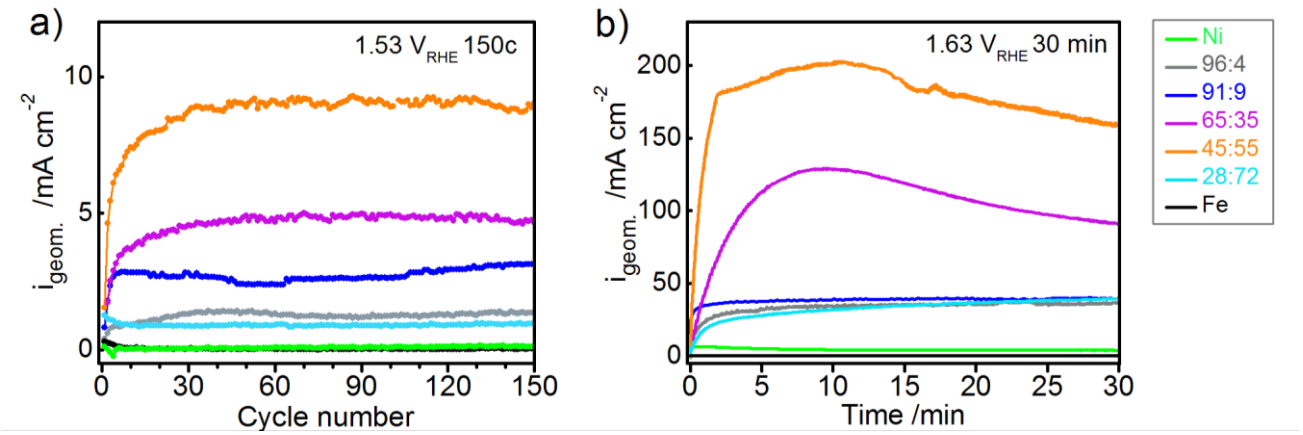

Figure S3. Evaluation of the OER activity during potentiodynamic and potentiostatic conditioning. **(a)** Geometric current densities ($i_{geom.}$) extracted at 1.53 V_{RHE} during the first 150 cycles, collected at a scan-rate of 100 mV/s. **(b)** Application of 1.63 V_{RHE} for 30 min according to the conditioning protocol for the quasi-in situ XAS measurements. The measurements in (b) were carried out at iR-corrected potentials. Measurements were carried out in RDE setup in 0.1 M KOH. The metal loading was ~ 10 µg Ni+Fe cm^{-2}. The catalyst composition ($Ni_{100-x}Fe_x$) is given as atomic %.

S1.4. Dynamic redox changes

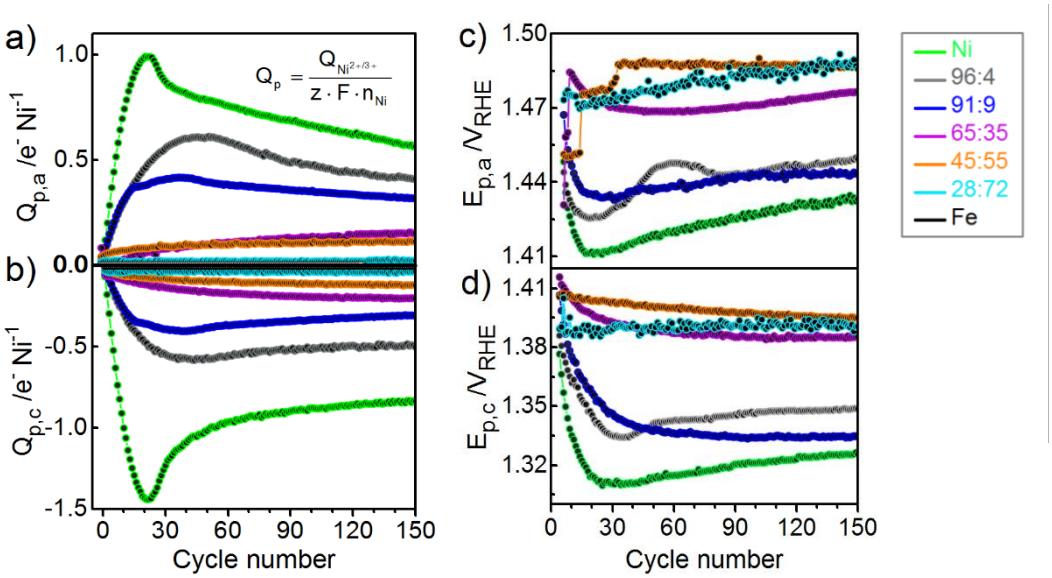

Figure S4. Evaluation of the $Ni(OH)_2$/NiOOH redox peak during the first 150 cycles; **a)** Anodic redox electrons ($Q_{p,a}$) defined as electrons transferred per Ni atoms (e^- Ni^{-1}) **(b)** Cathodic redox electrons ($Q_{p,c}$) **(c)** Anodic peak potential ($E_{p,a}$) **(d)** Cathodic peak potential ($E_{p,c}$). The value of Q was estimated based on the moles of Ni on the electrode determined prior to the measurement using ICP-OES. Measurements were carried out in RDE setup in 0.1 M KOH, at a scan-rate 100 mV/s at a rotation speed of 1600 rpm, and a metal loading of ~10 µg Ni+Fe cm^{-2}. The catalyst composition ($Ni_{100-x}Fe_x$) is indicated as atomic %.

S1.4.1. Mass corrected redox electrons

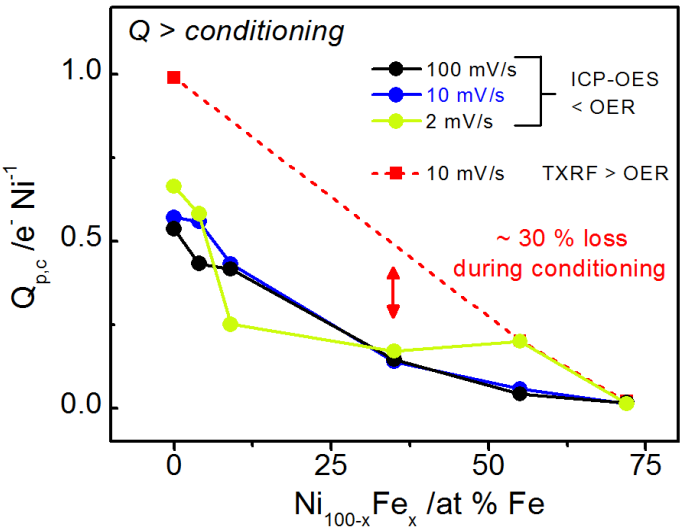

Figure S5. Evaluation of redox electrons (e^- Ni^{-1}) for the cathodic $Ni(OH)_2$/NiOOH redox peak estimated after application of 1.63V_{RHE} for 30 min in 0.1 M KOH. The integration was done at different scan-rates (100, 10, and 2 mV/s). The values of Q were estimated based on the total moles of Ni on the electrodes determined of as-prepared catalysts prior to the measurements using ICP-OES (< OER), and based on the total moles of Ni on the electrodes after the conditioning step determined using TXRF analysis (> OER).

S1.5. Impact of Fe impurities

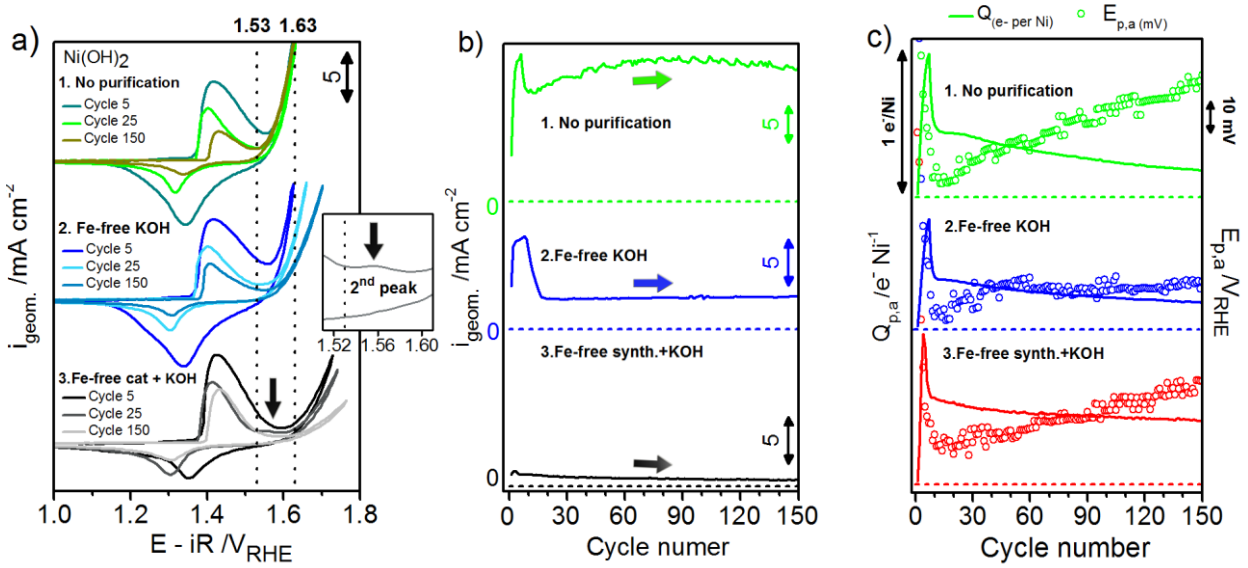

Figure S6. The Ni-catalyst (α-$Ni(OH)_2$) measured in 0.1 M KOH at different levels of Fe-impurities. **(a)** CVs of the Ni catalyst prepared without further purification measured in non-purified KOH (**1.)** Ni catalyst measured in Fe-free 0.1 M KOH (**2.)** Ni-catalyst prepared with purified chemicals measured in Fe-free 0.1 M KOH **(3.)**. Displayed CVs are cycle 5, 25 and 150. The inset shows an additional redox peak visible at ~1.56 V at cycle 25 **(b)** Geometric current density at 1.63 V_{RHE} during the first 150 cycles for the catalysts shown in (a). **(c)** Integrated anodic redox electrons (e^- per Ni) and the corresponding anodic peak position ($E_{p,a}$) during the first 150 cycles of the catalysts presented in (a). All measurements were recorded in RDE setup at 1600 rpm at a scan-rate of 100 mV/s using electrochemical cells made of polypropylene (Nalgene®) to avoid Fe-contamination. The geometric metal loading was ~ 5 µg Ni+Fe cm^{-2} determined by ICP-OES. All purifications were carried out according to the method reported by Trotochaud et al. [3].

S2. Differential Electrochemical Mass Spectrometry (DEMS)

S2.1. DEMS; Voltage domain

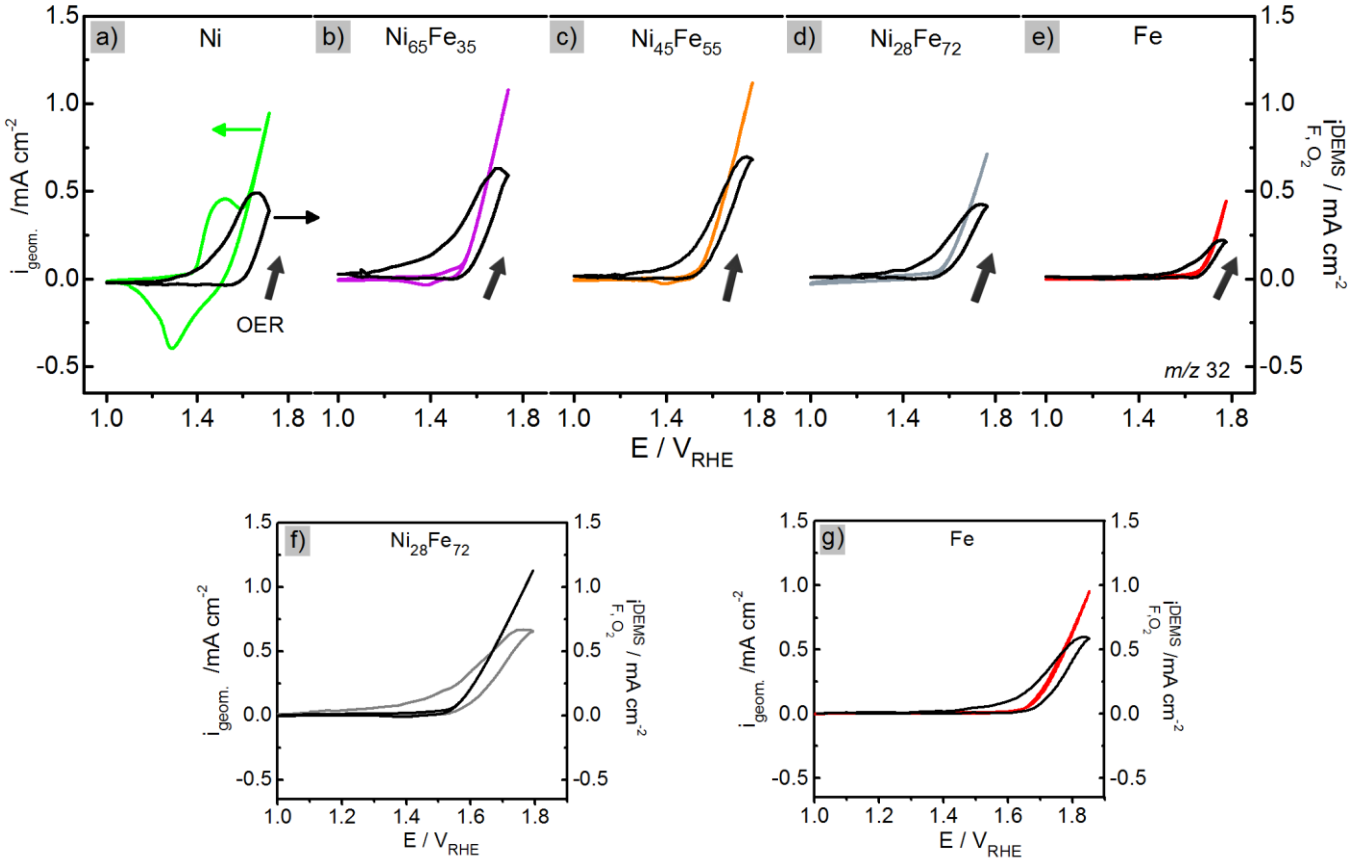

Figure S7. Differential electrochemical mass spectrometry (DEMS) measured in 0.1 M KOH using a dual thin-layer flow-cell. CVs were recorded at 50 mV/s between 1-1.8 V_{RHE} (before iR-comp.). **(a)** Ni catalyst **(b)** $Ni_{65}Fe_{35}$ **(c)** $Ni_{45}Fe_{55}$ **(d)** $Ni_{28}Fe_{72}$ **(e)** Fe catalyst. In order to reach higher current densities for some of the less active catalysts, CVs were recorded with increased scan-limits (~ 2.0 V_{RHE} before iR-comp.) of **(f)** $Ni_{28}Fe_{72}$ and **(g)** Fe catalyst. Geometric current density from the potentiostat (CVs) are shown as *colored lines* (left axis) and the mass spectrometric faradaic ion current of O_2 (*m/z* 32) are shown as *black lines* (right axis). The arrows pointing upwards indicate the scan direction of the DEMS trace. A calibration constant (*K**) was used to convert the integrated ion current to faradic current. More information is given in Experimental section 2.6. The catalyst composition ($Ni_{100-x}Fe_x$) is given as atomic %.

S2.2. DEMS; Time domain

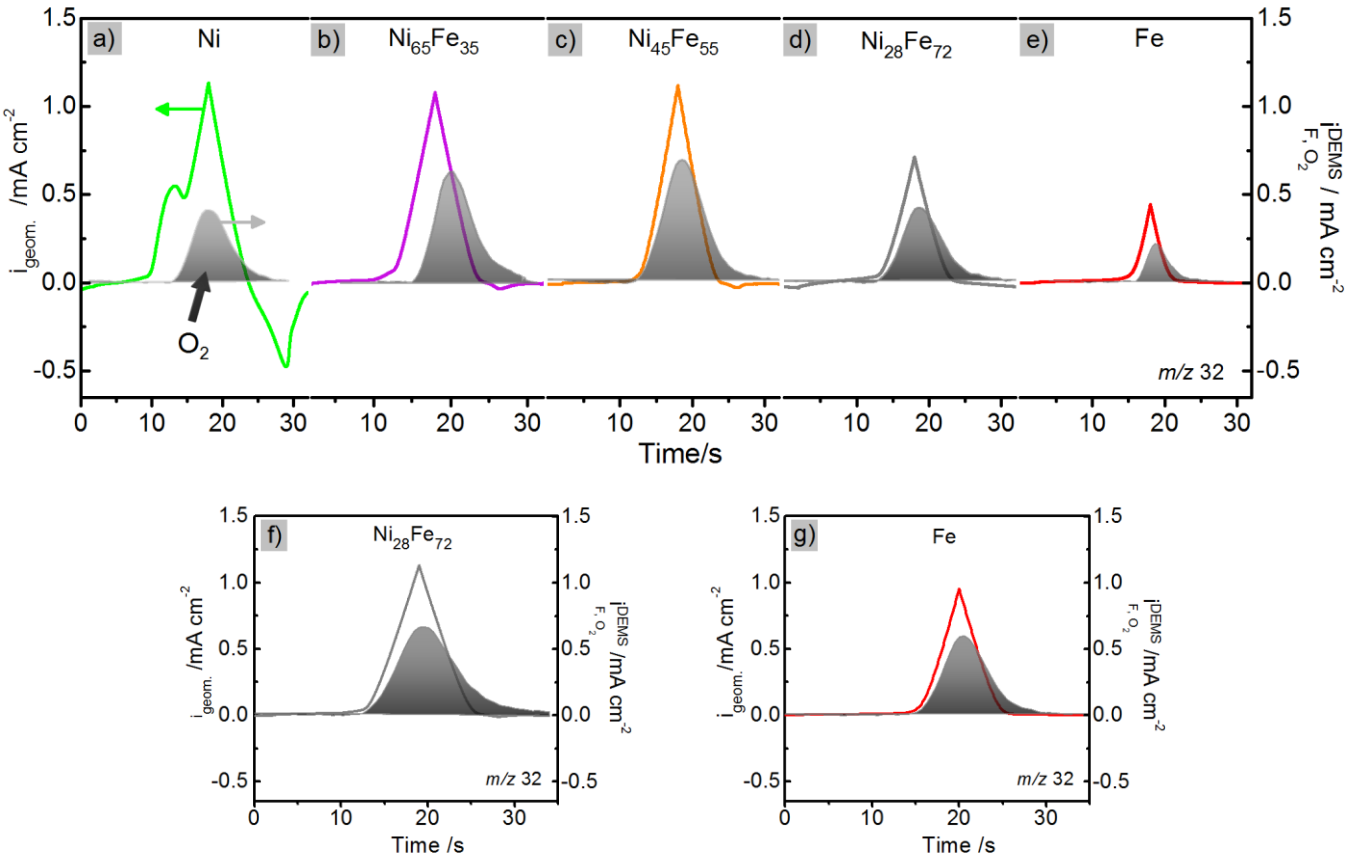

Figure S8. DEMS traces of the CVs in Fig. S7 shown in the time domain, measured in 0.1 M KOH using a dual thin-layer flow-cell. CVs were recorded at 50 mv/s between 1-1.8 V_{RHE} (before iR-comp.) and are shown for selected catalysts; **(a)** Ni **(b)** $Ni_{65}Fe_{35}$ **(c)** $Ni_{45}Fe_{55}$ **(d)** $Ni_{28}Fe_{72}$ **(e)** Fe. In order to reach higher current densities for less active catalysts CVs were recorded with increased scan-limits (~ 2.0 V_{RHE} before iR-comp.) of **(f)** $Ni_{28}Fe_{72}$ and **(g)** Fe catalyst. The CVs are shown as *colored lines* (left axis) and the mass spectrometric faradaic ion current of O_2 (*m/z* 32) as *black lines* (right axis). The arrows indicate the scan direction of the DEMS trace. A calibration constant (K^*) was used to convert the integrated ion current to faradic current. More information is given in Experimental section 2.6. The catalyst composition ($Ni_{100-x}Fe_x$) is given as atomic %.

S2.3. Faradaic efficiency - extended potential-limits

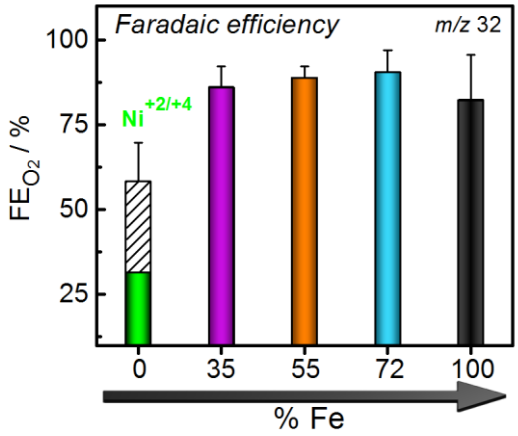

Figure S9. Faradaic efficiency (FE) for mixed Ni-Fe catalysts with efficiencies of the $Ni_{28}Fe_{72}$ and Fe-catalysts re-evaluated based on the measurements with extended scan-limits shown in Fig. S7f-g and S8f-g, scanned up to ~ 2.0 V_{RHE} (before iR-comp.) to reach higher current densities.

S2.4. Faradaic efficiency equations

$$\frac{Q_{F,jO2}^{DEMS}}{Q_{F,O2}^{DEMS} + Q_{F,Ni^{+3/+4}}} = 0.6 \quad \text{(S1)}$$

$$0.4\, Q_{F,O2}^{DEMS} = Q_{F,Ni^{+3/+4}} \quad \text{(S2)}$$

$$\frac{Q_{F,O2}^{DEMS}}{Q_{F,O2}^{DEMS} + Q_{F,Ni^{+2/+3}} + Q_{F,Ni^{+3/+4}}} = 0.33 \quad \text{(S3)}$$

$$1.6\, Q_{F,O2}^{DEMS} = Q_{F,Ni^{+2/+3}} \quad \text{(S4)}$$

$$\frac{Q_{F,Ni^{+3/+4}}}{Q_{F,Ni^{+2/+3}}} = \frac{1}{4} \quad \text{(S5)}$$

S3. X-ray diffraction

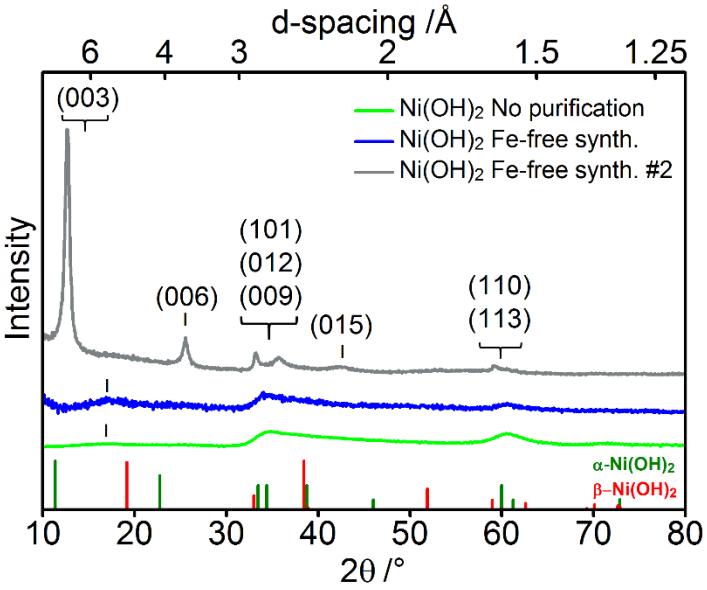

Figure S10. XRD of the as-prepared Ni catalyst; prepared with as-received chemicals (green curve), Fe-Free Ni catalyst prepared with purified chemicals (blue curve), and a slightly different Ni catalyst prepared with purified chemicals and a modified synthesis protocol (grey curve). Further details are given in the Experimental section 2.1. The lines at the bottom show reference patterns of α-$Ni(OH)_2$ (red, pdf # 00-038-0715) and β-$Ni(OH)_2$ (dark green, pdf # 01-074-2075). Removal of trace Fe (purification) was carried out according to the method reported by Trotochaud et al. [3].

S4. SEM-EDX elemental analysis

S4.1. SEM of Ni and Fe catalysts

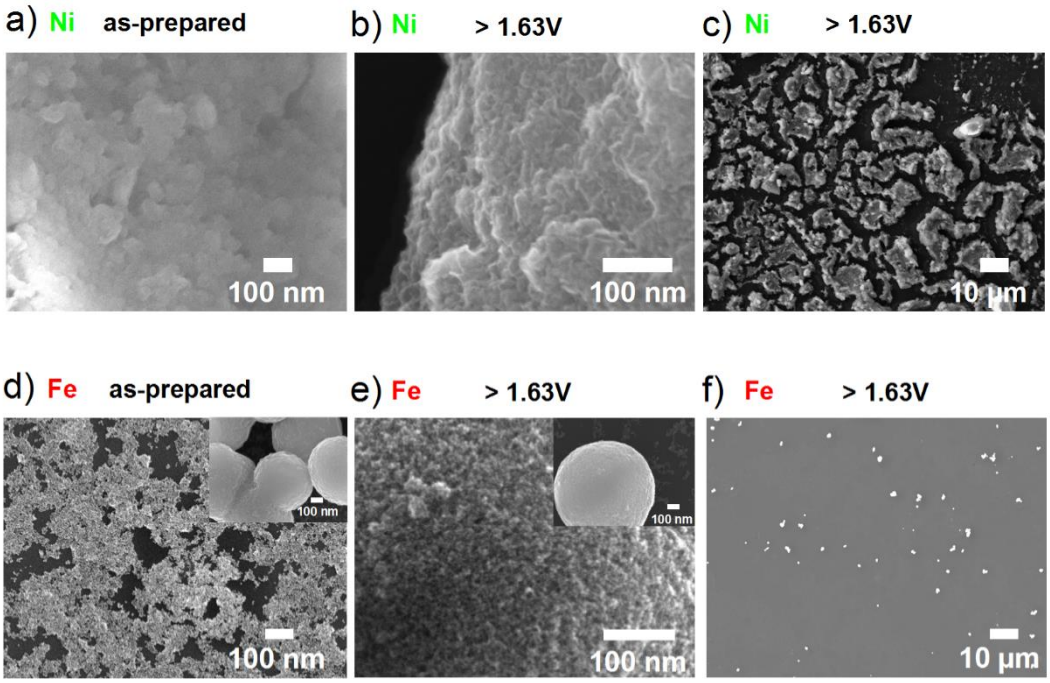

Figure S11. SEM images of catalysts drop-casted on glassy carbon electrodes; **(a)** as-prepared Ni catalyst **(b-c)** Ni catalyst after application of 1.63 V for 30 min in 0.1 M KOH (as received) shown at different magnifications. **(d)** As-prepared Fe catalyst. The inset shows large agglomerates of small Fe particles. **(e-f)** Fe catalyst after application of 1.63 V for 30 min in 0.1 M KOH (as received) shown at different magnifications. The inset in (d) shows a large Fe agglomerate.

S4.2. EDX elemental mapping of $Ni_{45}Fe_{55}$

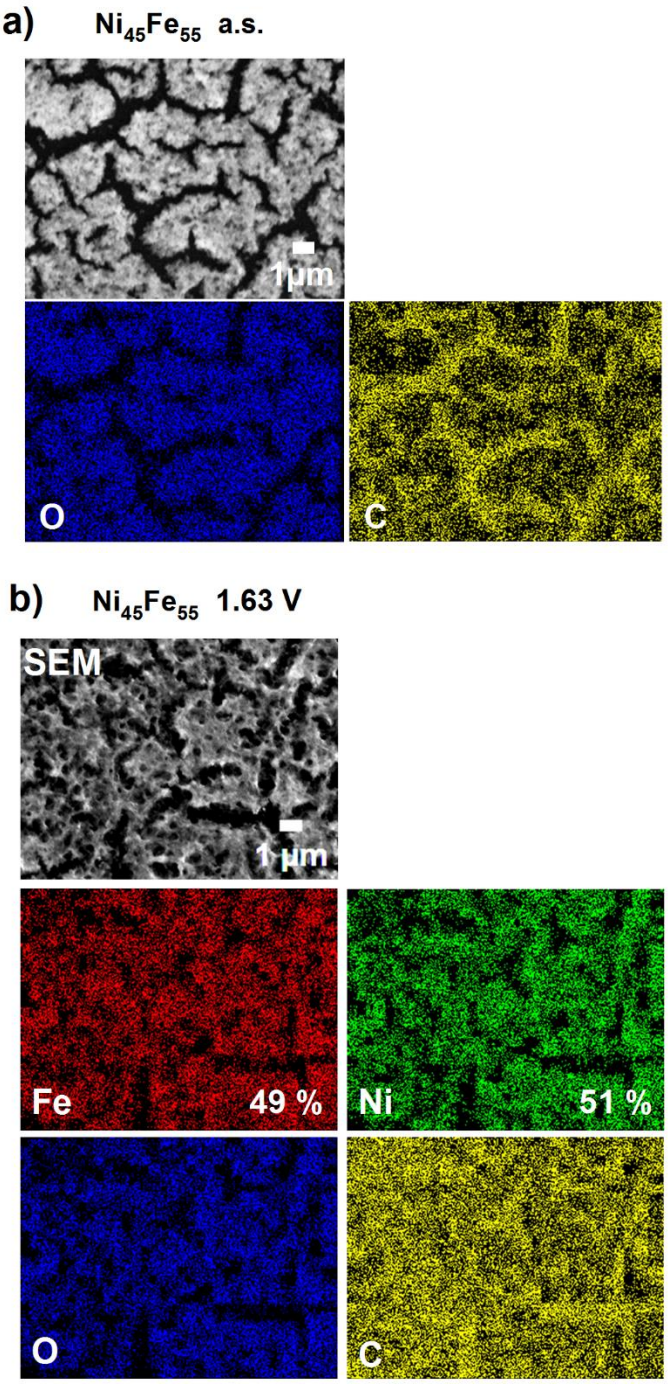

Figure S12. SEM images and EDX elemental mapping of the $Ni_{45}Fe_{55}$ catalyst drop casted on a glassy carbon electrode. **(a)** O and C content of the as-prepared catalyst **(b)** O, C, Ni, and Fe content of the catalyst shown in (a) after conditioning at 1.63 V for 30 min in 0.1 M KOH. The elements in the EDX mappings are indicated with colors; Ni (green), Fe (red), and O (blue), C (yellow).

S4.3. EDX line-scan analysis of $Ni_{45}Fe_{55}$

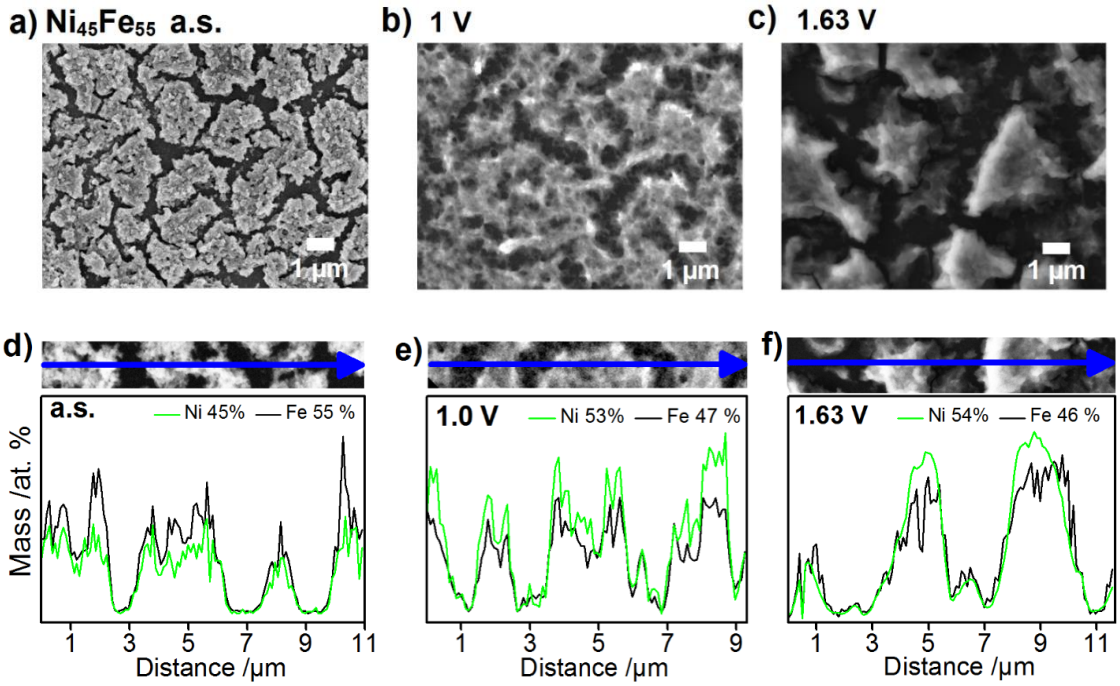

Figure S13. SEM images of the $Ni_{45}Fe_{55}$ catalysts drop-casted on glassy carbon electrodes **(a)** as-prepared catalyst (a.s.) **(b)** after application of 1.0 V_{RHE} for 30 min in 0.1 M KOH **(c)** after application of 1.63 V_{RHE} for 30 min in 0.1 M KOH. The catalysts in (a-c) were further analyzed using energy dispersive X-ray line-scan analysis to determine the atomic composition of Ni and Fe across a selected path (blue arrow) **(d)** as-prepared **(e)** conditioned at 1.0 V **(f)** conditioned at 1.63 V.

S5. Quasi-in situ X-ray absorption spectroscopy

S5.1. Ni and Fe XANES

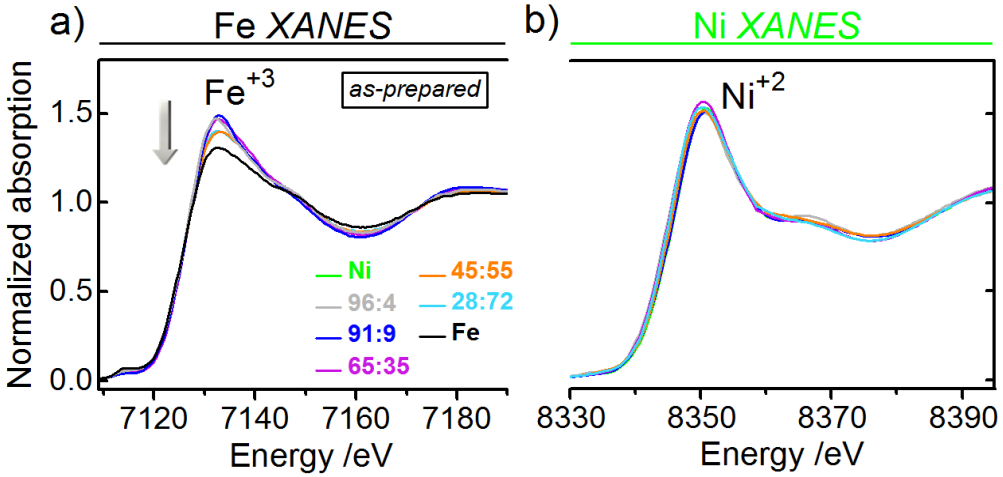

Figure S14. X-ray absorption near edge spectra (XANES) of as-prepared catalysts. **(a)** Fe *K*-edges **(b)** Ni *K*-edges. The catalyst composition, $Ni_{100-x}Fe_x$, is indicated as atomic % in the legend shown in (a) which applies to both Fe and Ni *K*-edges.

S5.2. Fourier transformed EXAFS

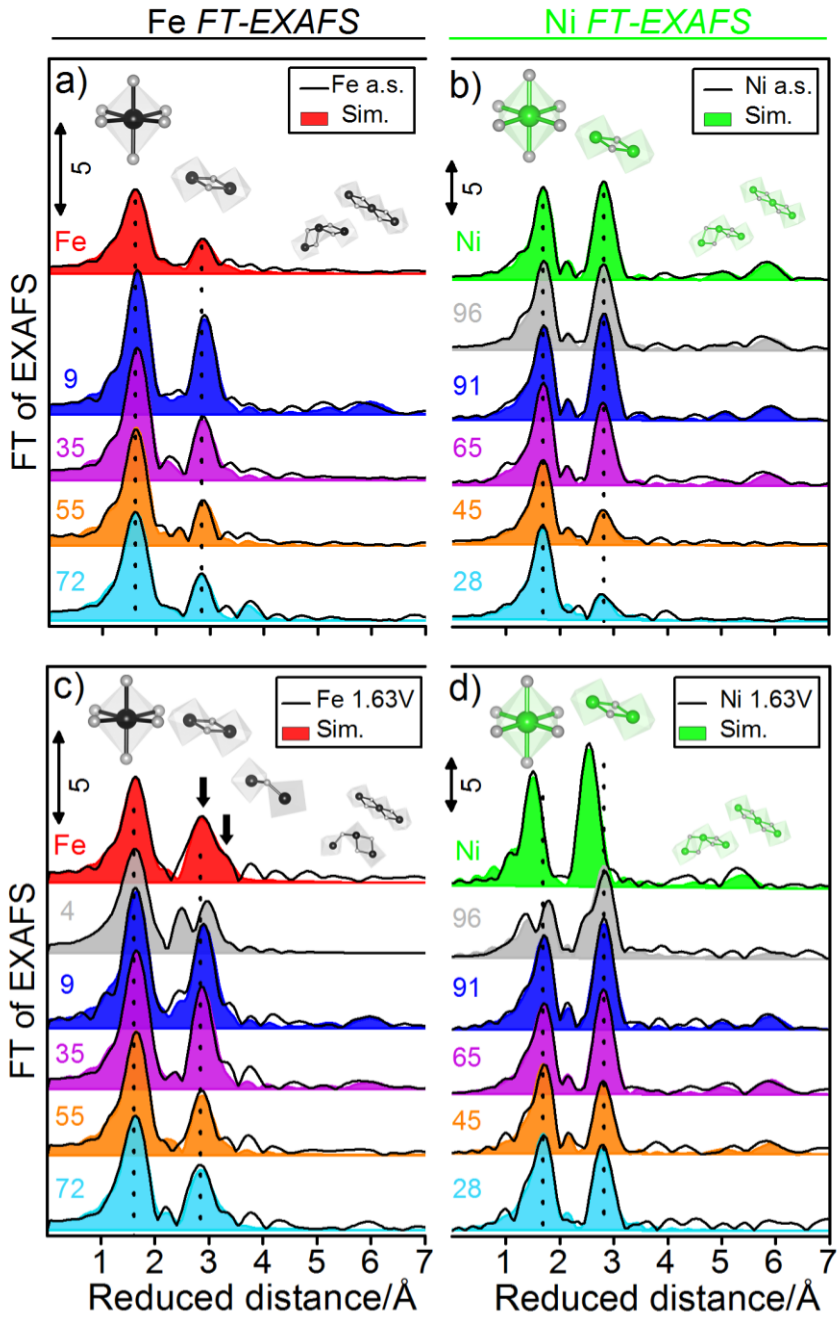

Figure S15. Fourier transformed k^3-weighted EXAFS spectra. Experimental data (*black curves*) and simulations (*colored shaded areas*) at the **(a)** Ni *K*-edge of as-prepared catalysts (a.s.) **(b)** Fe *K*-edge of as-prepared catalysts **(c)** Ni *K*-edge of catalysts freeze-quenched at 1.63 V **(d)** Fe *K*-edge of catalysts frozen at 1.63 V. The catalyst composition, $Ni_{100-x}Fe_x$, is indicated as atomic % Fe or Ni for the respective edge. Catalysts were freeze quenched under applied potential after conditioning at the given potential for 30 min in 0.1 M KOH. Fit parameters are listed in Tables S2-S5.

S5.3. Extended X-ray absorption spectroscopy

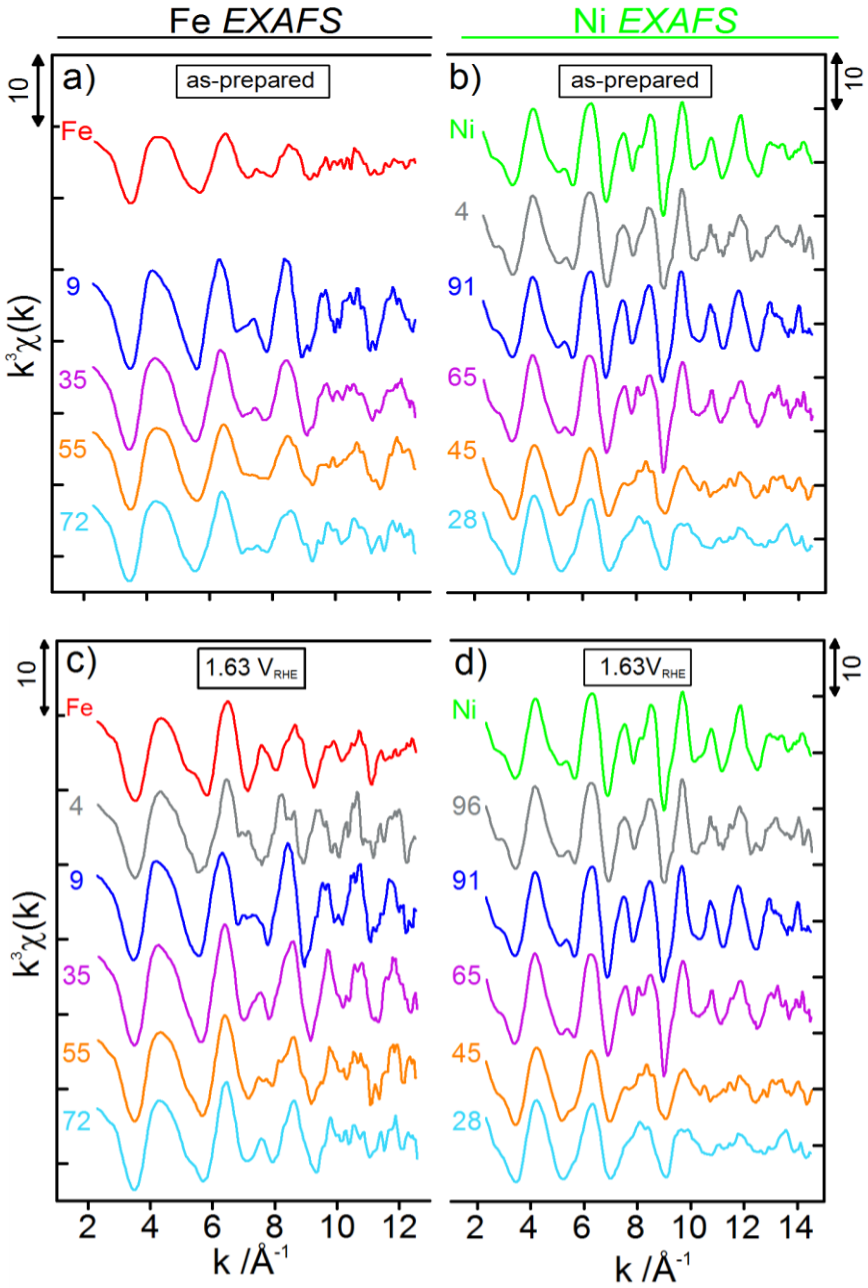

Figure S16. Extended X-ray absorption fine structure (EXAFS) **(a)** Fe *K*-edge of as-prepared catalysts **(b)** Ni *K*-edge of as-prepared catalysts **(c)** Fe *K*-edge of catalysts freeze quenched at 1.63 V. **(d)** Ni *K*-edge of catalysts freeze quenched at 1.63 V. The catalyst composition ($Ni_{100-x}Fe_x$) is indicated as atomic % Fe or Ni for the respective *K*-edges. Catalysts were frozen under applied potential after conditioning at the given potential for 30 min in 0.1 M KOH.

S5.4. XAS trends vs. catalyst composition

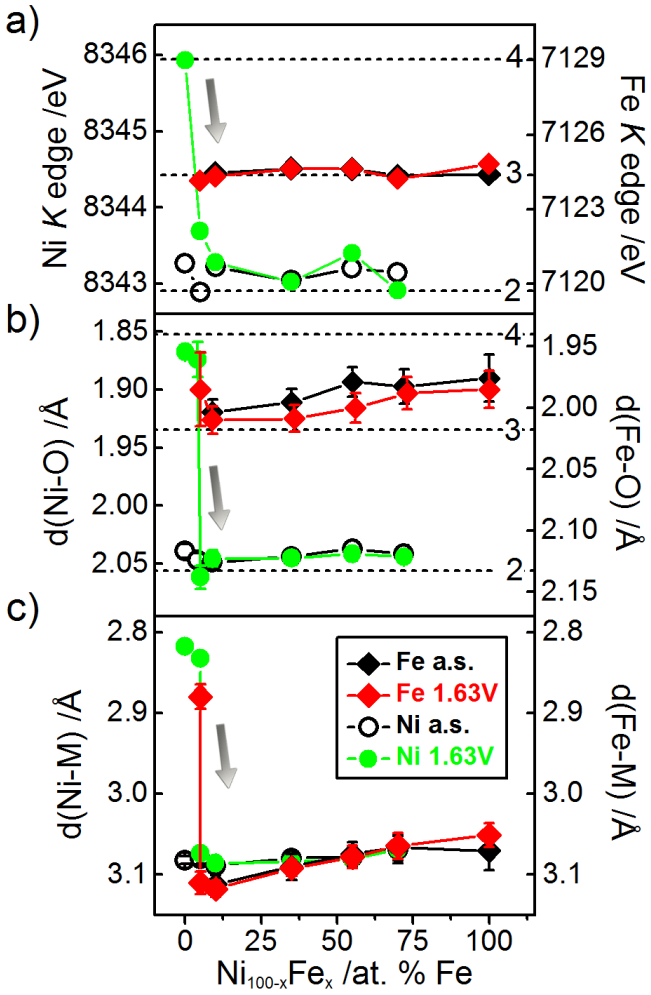

Figure S17. Trends obtained from the fitted XAS spectra as a function of Fe-content **(a)** Ni and Fe *K*-edge positions. **(b)** M-O coordination distances **(c)** M-M coordination distances. The dotted lines in (a)-(b) indicate the oxidation states determined from reference compounds presented in Tables S8-9. The values in (b-c) were obtained by the fitting k^3-weighted EXAFS oscillations in k-space between 2.6-14 $Å^{-1}$ at the Ni *K*-edge and 2.6-12.5 $Å^{-1}$ at the Fe *K*-edge. Fit parameters are listed in Tables S1-S5.

S5.5. Quasi-in situ XAS at different potentials

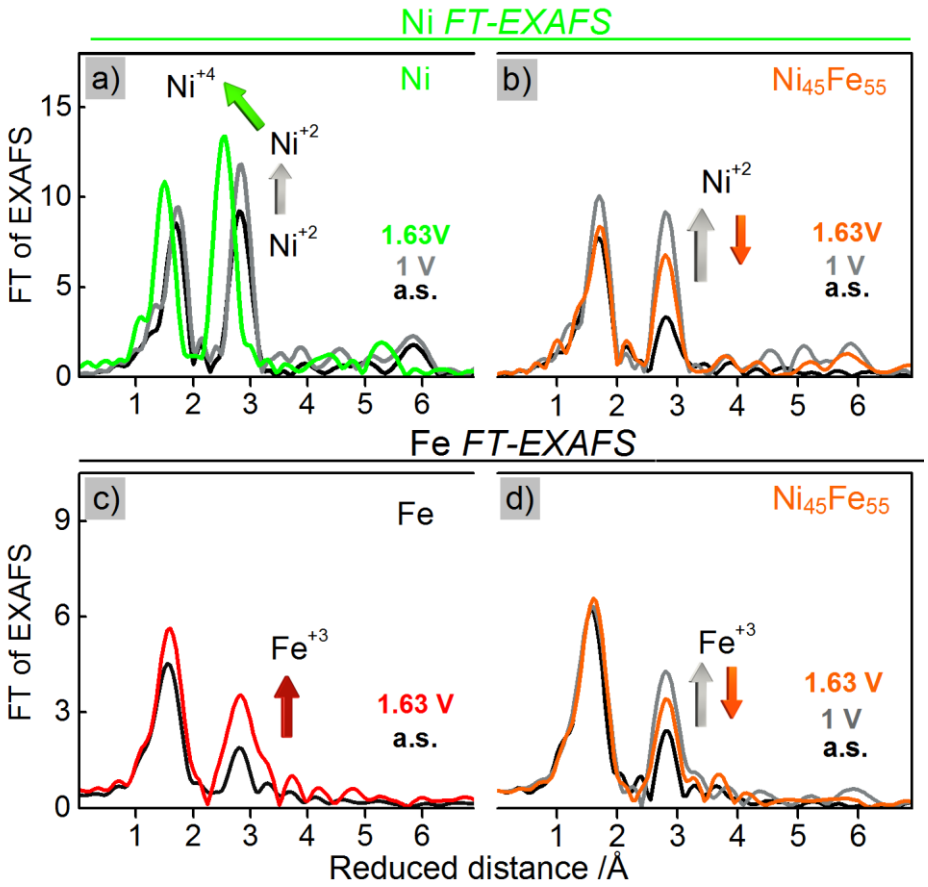

Figure S18. The k^3-weighted FT-EXAFS at the Ni *K*-edges of the **(a)** Ni catalyst and **(b)** $Ni_{45}Fe_{55}$ catalyst, and at the Fe *K*-edges of the **(c)** Fe catalyst and **(d)** $Ni_{45}Fe_{55}$. Data is shown for the as-prepared catalysts (a.s., *black curves*), and catalysts frozen at 1.0 V_{RHE} (*grey curves*), and catalysts frozen at 1.63 V_{RHE} (*colored curves*). Catalysts were frozen at the given potential after conditioning for 30 min in 0.1 M KOH.

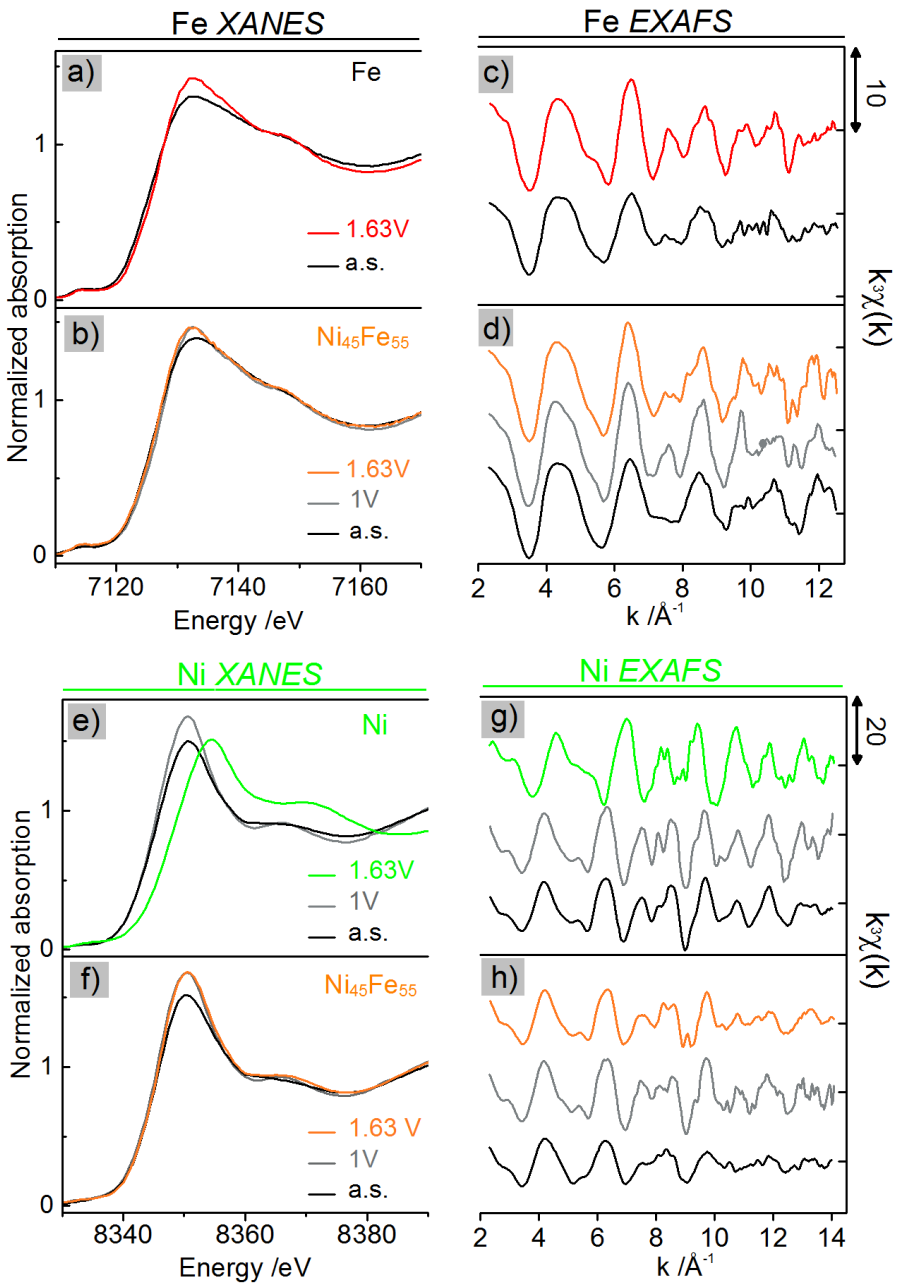

Figure S19. Fe *K*-edge XANES of **(a)** Fe catalyst and **(b)** $Ni_{45}Fe_{55}$, and Fe EXAFS oscillations of **(c)** Fe catalyst and **(d)** $Ni_{45}Fe_{55}$**.** Ni *K*-edge XANES of **(e)** Ni catalyst and **(f)** $Ni_{45}Fe_{55}$, and Ni EXAFS oscillations of **(g)** Ni catalyst and **(h)** $Ni_{45}Fe_{55}$**.** Shown are as-prepared catalysts (a.s., *black curves*), freeze quenched at 1.0 V_{RHE} (*grey curves*), and freeze quenched at 1.63 V_{RHE} (*colored curves*). The catalyst composition, $Ni_{100-x}Fe_x$ is given as at. %. Catalysts were freeze-quenched under applied potential after conditioning at the given potential for 30 min in 0.1 M KOH.

S6. XAS simulations & tables of fit parameters

The k^3 weighted EXAFS spectra were extracted using E_0 = 8333 eV for the Ni *K*-edge and E_0 = 7117 eV for the Fe *K*-edge. The simulations were carried out using in-house software (SimX) with phase functions generated from atomic coordinates of layered α-$Ni(OH)_2$, γ-NiOOH and γ/α-FeOOH using FEFF version 9.1 with self-consistent field option switched on[4,5]. An amplitude reduction factor S_0^2 of 0.85 was used at both the Ni and Fe *K*-edges. The fits were carried out in k-space with a range of 25-750 eV above E_0 (k-range of 2.6 -14 $Å^{-1}$) for the Ni *K*-edge and 25-600 eV (k-range of 2.6-12.5 $Å^{-1}$) for the Fe *K*-edge. A global fit approach was used, where Debye-Waller factors of each Ni/Fe-M shell had the same value for all as-prepared catalysts and another value for all freeze-quenched catalysts. To account for variations in catalyst composition of the mixed Ni-Fe catalysts arising from variations in the phase functions associated with either Ni or Fe absorbers, each M-M shell was split into a M-Ni and M-Fe shell with a ratio between them set equal to the actual atomic Ni:Fe ratio determined by ICP-OES. To simulate the FT peaks at reduced distance 5-6 Å, a shell corresponding to three collinearly arranged metal atoms, Ni/Fe-M-M, was added to the simulation of some of the catalysts, with a shell distance set equal to double the corresponding Ni/Fe-M distance; the shell included multiple-scattering contributions and contributions from three metal atoms arranged at an angle of 120° (see the insets of Figure S15 for the corresponding structural motifs). Two additional shells at 2.86 Å and at 3.45 Å were required in order to achieve a reasonable fit quality in the freeze-quenched catalysts and were included at both Ni and Fe *K*-edges; the two distances had the same value in all freeze-quenched catalysts in the global fit. The fit parameters were optimized by the least squares method using a Levenberg-Marquardt algorithm; parameter errors were determined from the covariance matrix of the fit and correspond to 68 % confidence intervals.

S6.1. Tables of XAS parameters

Table S1. Ni and Fe *K*-edge positions of as-prepared catalysts (a.s.) and catalysts freeze-quenched at 1.63 V after conditioning for 30 min in 0.1 M KOH, with corresponding average oxidation states determined from a comparison to reference compounds presented in Tables S8-9.

$Ni_{100-x}Fe_x$ /at. %	Ni *K*-edge				Fe *K*-edge			
	Pos. (a.s.) /eV	Ox. state	Pos. (1.63 V) /eV	Ox. state	Pos. (a.s.) /eV	Ox. state	Pos. (1.63V) /eV	Ox. state
$Ni_{100}Fe_0$	8343.3	2.2	8345.9	4.0	-	-	-	-
$Ni_{96}Fe_4$	8342.9	2.0	8343.7	2.6	-	-	7124.2	2.9
$Ni_{91}Fe_9$	8343.2	2.2	8343.3	2.3	7124.5	3.0	7124.3	3.0
$Ni_{65}Fe_{35}$	8343.0	2.1	8343.0	2.1	7124.7	3.1	7124.6	3.1
$Ni_{45}Fe_{55}$	8343.4	2.2	8343.3	2.3	7124.6	3.1	7124.7	3.1
$Ni_{28}Fe_{72}$	8343.2	2.2	8342.9	2.0	7124.4	3.0	7124.2	3.0
Ni_0Fe_{100}	-	-	-	-	7124.4	3.0	7124.9	3.1

K-edge positions (pos.) were obtained by the integral method reported by Dau et al.[6] The catalyst composition is given as atomic %, rounded to the nearest integer.

Table S2. Fe *K*-edge EXAFS simulation parameters of as-prepared catalysts (a.s.). The fitted k-range was 2.6-12.5 $Å^{-1}$.

Fe *K*-edge as-prepared						
$Ni_{100-x}Fe_x$	Shell	R /Å	CN	σ /Å	ΔE_0 /eV	R_f
Ni_0Fe_{100}	Fe-O	1.98 ± 0.02	4.4 ± 0.9	0.10 ± 0.02	0.4	14.5
	Fe-M	3.07 ± 0.02	2.6 ± 1.1	0.09 ± 0.01*		
$Ni_{91}Fe_9$	Fe-O	2.00 ± 0.01	5.9 ± 0.8	0.08 ± 0.01	0.8	11.7
	Fe-M	3.11 ± 0.01	6.0 ± 1.6	0.09 ± 0.01*		
	Fe-M-M	6.22†	1.5 ± 1.2	0.09 ± 0.01*		
$Ni_{65}Fe_{35}$	Fe-O	2.00 ± 0.01	5.6 ± 0.8	0.08 ± 0.01	0.8	12.2
	Fe-M	3.09 ± 0.02	3.5 ± 0.8	0.09 ± 0.01*		
$Ni_{45}Fe_{55}$	Fe-O	1.98 ± 0.01	4.8 ± 0.7	0.08 ± 0.01	0.4	15.2
	Fe-M	3.08 ± 0.02	3.8 ± 0.7	0.09 ± 0.01*		
$Ni_{28}Fe_{72}$	Fe-O	1.98 ± 0.01	5.3 ± 0.9	0.09 ± 0.01	0.5	16.7
	Fe-M	3.07 ± 0.02	3.0 ± 0.9	0.09 ± 0.01*		

* Debye-Waller parameters (σ) of Fe-M shells that had the same value in a global fit approach.

† Coordination distance of the Fe-M-M shell was set equal to double the Fe-M distance.

Debye-Waller parameters, coordination distances (R) and coordination numbers (CN) were kept unrestricted unless indicated. Catalyst composition is given as atomic %, rounded to the nearest integer.

Table S3. Ni *K*-edge EXAFS simulation parameters of as-prepared catalysts (a.s.). The fitted k-range was 2.6-14 $Å^{-1}$.

Ni *K*-edge as-prepared						
$Ni_{100-x}Fe_x$	Shell	R /Å	CN	σ /Å	ΔE_0 /eV	R_f
$Ni_{100}Fe_0$	Ni-O	2.04 ± 0.01	5.2 ± 0.5	0.07 ± 0.01	1.4	13.1
	Ni-M	3.08 ± 0.01	6.3 ± 0.4	0.07 ± 0.01*		
	Ni-M-M	6.16†	2.6 ± 0.6	0.07 ± 0.01*		
$Ni_{96}Fe_4$	Ni-O	2.05 ± 0.01	5.6 ± 0.5	0.07 ± 0.01	1.9	14.4
	Ni-M	3.08 ± 0.01	5.5 ± 0.4	0.07 ± 0.01*		
	Ni-M-M	6.16†	1.9 ± 0.6	0.07 ± 0.01*		
$Ni_{91}Fe_9$	Ni-O	2.05 ± 0.01	5.7 ± 0.5	0.07 ± 0.01	1.7	9.9
	Ni-M	3.09 ± 0.01	6.6 ± 0.4	0.07 ± 0.01*		
	Ni-M-M	6.19†	2.2 ± 0.6	0.07 ± 0.01*		
$Ni_{65}Fe_{35}$	Ni-O	2.04 ± 0.01	6.3 ± 0.5	0.07 ± 0.01	1.6	15.7
	Ni-M	3.08 ± 0.01	5.5 ± 0.3	0.07 ± 0.01*		
	Ni-M-M	6.16†	1.8 ± 0.6	0.07 ± 0.01*		
$Ni_{45}Fe_{55}$	Ni-O	2.04 ± 0.01	5.7 ± 0.5	0.08 ± 0.01	1.4	16.2
	Ni-M	3.08 ± 0.01	2.3 ± 0.2	0.07 ± 0.01*		
$Ni_{28}Fe_{72}$	Ni-O	2.04 ± 0.01	6.4 ± 0.5	0.08 ± 0.01	1.3	20.2
	Ni-M	3.07 ± 0.02	1.8 ± 0.3	0.07 ± 0.01*		

* Debye-Waller parameters of Ni-M shells that had the same value in a global fit approach.

† Coordination distances of the Ni-M-M shell were set equal to double the corresponding Ni-M distance.

Debye-Waller parameters, Coordination distances (R) and coordination numbers (CN) were kept unrestricted. Catalyst composition is given as atomic %, rounded to the nearest integer.

Table S4. Fe *K*-edge EXAFS simulation parameters of catalysts freeze quenched at 1.63 V_{RHE} after conditioning at the given potential for 30 min in 0.1 M KOH. The fitted k-range was 2.6-12.5 $Å^{-1}$.

Fe *K*-edge at 1.63 V_{RHE}						
$Ni_{100-x}Fe_x$	Shell	R /Å	CN	σ /Å	ΔE_0 /eV	R_f
Ni_0Fe_{100}	Fe-O	1.98 ± 0.02	5.0 ± 0.9	0.09 ± 0.01	1.2	20.1
	Fe-M	3.05 ± 0.02	4.9 ± 1.0	0.08 ± 0.01*		
	Fe-M	2.86 ± 0.02 [a]	0.5 ± 0.7	0.08 ± 0.01*		
	Fe-M	3.45 ± 0.02 [b]	1.8 ± 0.9	0.08 ± 0.01*		
$Ni_{96}Fe_4$	Fe-O	1.99 ± 0.03	5.8 ± 1.0	0.10 ± 0.01	0.7	23.0
	Fe-M	3.11 ± 0.01	3.7 ± 0.3	0.08 ± 0.01*		
	Fe-M	2.88 ± 0.02	2.9 ± 0.3	0.08 ± 0.01*		
	Fe-M	3.45 ± 0.02 [b]	0.0 ± 5.1	0.08 ± 0.01*		
$Ni_{91}Fe_9$	Fe-O	2.01 ± 0.01	6.3 ± 0.8	0.09 ± 0.01	0.7	15.9
	Fe-M	3.12 ± 0.01	6.7 ± 1.0	0.08 ± 0.01*		
	Fe-M-M	6.24[†]	1.2 ± 1.1	0.08 ± 0.01*		
	Fe-M	2.86 ± 0.02 [a]	1.2 ± 0.8	0.08 ± 0.01*		
	Fe-M	3.45 ± 0.02 [b]	0.4 ± 0.8	0.08 ± 0.01*		
$Ni_{65}Fe_{35}$	Fe-O	2.01 ± 0.01	6.2 ± 0.8	0.09 ± 0.01	1.9	14.4
	Fe-M	3.09 ± 0.01	6.5 ± 0.8	0.08 ± 0.01*		
	Fe-M-M	6.19[†]	0.6 ± 0.8	0.08 ± 0.01*		
	Fe-M	2.86 ± 0.02 [a]	1.1 ± 0.8	0.08 ± 0.01*		
	Fe-M	3.45 ± 0.02 [b]	0.2 ± 0.8	0.08 ± 0.01*		
$Ni_{45}Fe_{55}$	Fe-O	2.00 ± 0.01	5.2 ± 0.8	0.08 ± 0.01	1.7	17.9
	Fe-M	3.08 ± 0.01	3.7 ± 0.5	0.08 ± 0.01*		
	Fe-M	2.86 ± 0.02 [a]	0.5 ± 0.7	0.08 ± 0.01*		
	Fe-M	3.45 ± 0.02 [b]	0.3 ± 0.8	0.08 ± 0.01*		
$Ni_{28}Fe_{72}$	Fe-O	1.99 ± 0.01	5.4 ± 0.8	0.09 ± 0.01	0.8	19.4
	Fe-M	3.07 ± 0.02	3.5 ± 0.7	0.08 ± 0.01*		
	Fe-M	2.86 ± 0.02 [a]	0.0 ± 0.7	0.08 ± 0.01*		
	Fe-M	3.45 ± 0.02 [b]	1.2 ± 0.8	0.08 ± 0.01*		

* Debye-Waller parameters (σ) of Fe-M shells that ad the same value in a global fit approach.

[†] Coordination distances of the Fe-M-M shell were set equal to double the corresponding Fe-M distance.

The coordination distances (R) of two additional Fe-M shells, [a] and [b], had the same value in all freeze-quenched catalysts in the global fit.

Debye-Waller parameters, coordination distances and coordination numbers (CN) were kept unrestricted unless indicated. Catalyst composition is given as atomic %, rounded to the nearest integer.

Table S5. Ni *K*-edge EXAFS simulation parameters of catalysts freeze quenched at 1.63 V_{RHE} after conditioning at the given potential for 30 min in 0.1 M KOH. The fitted k-range was 2.6-14 $Å^{-1}$.

Ni *K*-edge at 1.63 V_{RHE}						
$Ni_{100-x}Fe_x$	Shell	R /Å	CN	σ /Å	ΔE_0 /eV	R_f
$Ni_{100}Fe_0$	Ni-O	1.88 ± 0.01	4.9 ± 0.3	0.06 ± 0.01	2.6	15.2
	Ni-M	2.82 ± 0.01	6.3 ± 0.2	0.06 ± 0.02*		
	Ni-M-M	5.64†	1.2 ± 0.3	0.06 ± 0.02*		
	Ni-M	3.45 ± 0.02 [b]	0.1 ± 0.3	0.06 ± 0.02*		
$Ni_{96}Fe_4$	Ni-O	2.06 ± 0.01	4.1 ± 0.2	0.07 ± 0.01	1.4	24.4
	Ni-O	1.87 ± 0.02	1.9 ± 0.2	0.07 ± 0.01		
	Ni-M	3.07 ± 0.01	4.0 ± 0.2	0.06 ± 0.02*		
	Ni-M	2.83 ± 0.01	2.0 ± 0.2	0.06 ± 0.02*		
	Ni-M	3.45 ± 0.02 [b]	0.0 ± 0.4	0.06 ± 0.02*		
$Ni_{91}Fe_9$	Ni-O	2.04 ± 0.01	6.6 ± 0.5	0.07 ± 0.01	1.1	15.5
	Ni-M	3.09 ± 0.01	5.4 ± 0.3	0.06 ± 0.02*		
	Ni-M-M	6.17†	1.6 ± 0.5	0.06 ± 0.02*		
	Ni-M	2.86 ± 0.02 [a]	0.1 ± 0.3	0.06 ± 0.02*		
	Ni-M	3.45 ± 0.02 [b]	0.4 ± 0.4	0.06 ± 0.02*		
$Ni_{65}Fe_{35}$	Ni-O	2.05 ± 0.01	6.6 ± 0.6	0.08 ± 0.01	1.5	16.6
	Ni-M	3.08 ± 0.01	4.9 ± 0.2	0.06 ± 0.02*		
	Ni-M-M	6.17†	1.8 ± 0.5	0.06 ± 0.02*		
	Ni-M	2.86 ± 0.02 [a]	0.0 ± 0.3	0.06 ± 0.02*		
	Ni-M	3.45 ± 0.02 [b]	0.2 ± 0.4	0.06 ± 0.02*		
$Ni_{45}Fe_{55}$	Ni-O	2.04 ± 0.01	5.6 ± 0.5	0.07 ± 0.01	2.1	24.8
	Ni-M	3.08 ± 0.01	3.3 ± 0.1	0.06 ± 0.02*		
	Ni-M-M	6.16†	1.3 ± 0.5	0.06 ± 0.02*		
	Ni-M	2.86 ± 0.02 [a]	0.0 ± 0.3	0.06 ± 0.02*		
	Ni-M	3.45 ± 0.02 [b]	0.3 ± 0.4	0.06 ± 0.02*		
$Ni_{28}Fe_{72}$	Ni-O	2.05 ± 0.01	6.7 ± 0.5	0.08 ± 0.01	0.8	23.5
	Ni-M	3.07 ± 0.01	4.4 ± 0.2	0.06 ± 0.02*		
	Ni-M	2.86 ± 0.02 [a]	0.0 ± 0.3	0.06 ± 0.02*		
	Ni-M	3.45 ± 0.02 [b]	0.8 ± 0.4	0.06 ± 0.02*		

* Debye-Waller parameters of Ni-M shells that had the same value in a global fit approach.

† Coordination distances of the Ni-M-M shell were set equal to double the corresponding Ni-M distance.

The distances of two additional Ni-M shells, [a] and [b], had the same value in all freeze-quenched catalysts in the global fit. Debye-Waller parameters, coordination distances (R) and coordination numbers (CN) were kept unrestricted unless indicated. Catalyst composition is given as atomic %, rounded to the nearest integer.

Table S6. Fe *K*-edge EXAFS simulation parameters of catalysts freeze quenched at 1.0 V_{RHE} after conditioning at the given potential for 30 min in 0.1 M KOH. The fitted k-range was 2.6-12.5 $Å^{-1}$.

Fe *K*-edge at 1.0 V_{RHE}						
$Ni_{100-x}Fe_x$	**Shell**	**R /Å**	**CN**	**σ /Å**	**ΔE_0 /eV**	**R_f**
$Ni_{91}Fe_9$	Fe-O	2.01 ± 0.01	5.9 ± 0.8	0.09 ± 0.01	0.4	16.1
	Fe-M	3.12 ± 0.01	4.9 ± 0.9	0.08 ± 0.01*		
	Fe-M-M	6.24†	2.1 ± 1.1	0.08 ± 0.01*		
$Ni_{45}Fe_{55}$	Fe-O	1.99 ± 0.01	5.9 ± 0.9	0.09 ± 0.01	1.0	13.6
	Fe-M	3.08 ± 0.01	3.5 ± 0.5	0.08 ± 0.01*		
	Fe-M-M	6.16†	0.9 ± 0.7	0.08 ± 0.01*		

* Debye-Waller parameters of Fe-M shells that had the same value in a global fit approach.

† Coordination distances of the Fe-M-M shell were set equal to double the corresponding Fe-M distance.

Debye-Waller parameters, coordination distances (R) and coordination numbers (CN) were kept unrestricted unless indicated. Catalyst composition is given as atomic %, rounded to the nearest integer.

Table S7. Ni *K*-edge EXAFS simulation parameters of catalysts freeze quenched at 1.0 V_{RHE} after conditioning at the given potential for 30 min in 0.1 M KOH. The fitted k-range was 2.6-14 $Å^{-1}$.

Ni *K*-edge at 1.0 V_{RHE}						
$Ni_{100-x}Fe_x$	**Shell**	**R /Å**	**CN**	**σ /Å**	**ΔE_0 /eV**	**R_f**
$Ni_{100}Fe_0$	Ni-O	2.06 ± 0.01	6.0 ± 0.4	0.07 ± 0.01	3.2	19.5
	Ni-M	3.09 ± 0.01	6.0 ± 0.4	0.06 ± 0.01*		
	Ni-M-M	6.18†	2.5 ± 0.5	0.06 ± 0.01*		
$Ni_{91}Fe_9$	Ni-O	2.04 ± 0.01	6.2 ± 0.5	0.07 ± 0.01	1.5	16.3
	Ni-M	3.09 ± 0.01	5.1 ± 0.3	0.06 ± 0.01*		
	Ni-M-M	6.17†	1.7 ± 0.5	0.06 ± 0.01*		
$Ni_{45}Fe_{55}$	Ni-O	2.05 ± 0.01	6.2 ± 0.4	0.07 ± 0.01	2.5	20.7
	Ni-M	3.08 ± 0.01	6.2 ± 0.7	0.06 ± 0.01*		
	Ni-M-M	6.17†	2.6 ± 0.4	0.06 ± 0.01*		

* Debye-Waller parameters of Ni-M shells that had the same value in a global fit approach.

† Coordination distances of the Ni-M-M shell were set equal to double the corresponding Ni-M distance.

Debye-Waller parameters, coordination distances (R) and coordination numbers (CN) were kept unrestricted unless indicated. Catalyst composition is given as atomic %, rounded to the nearest integer.

S6.2. Structural models

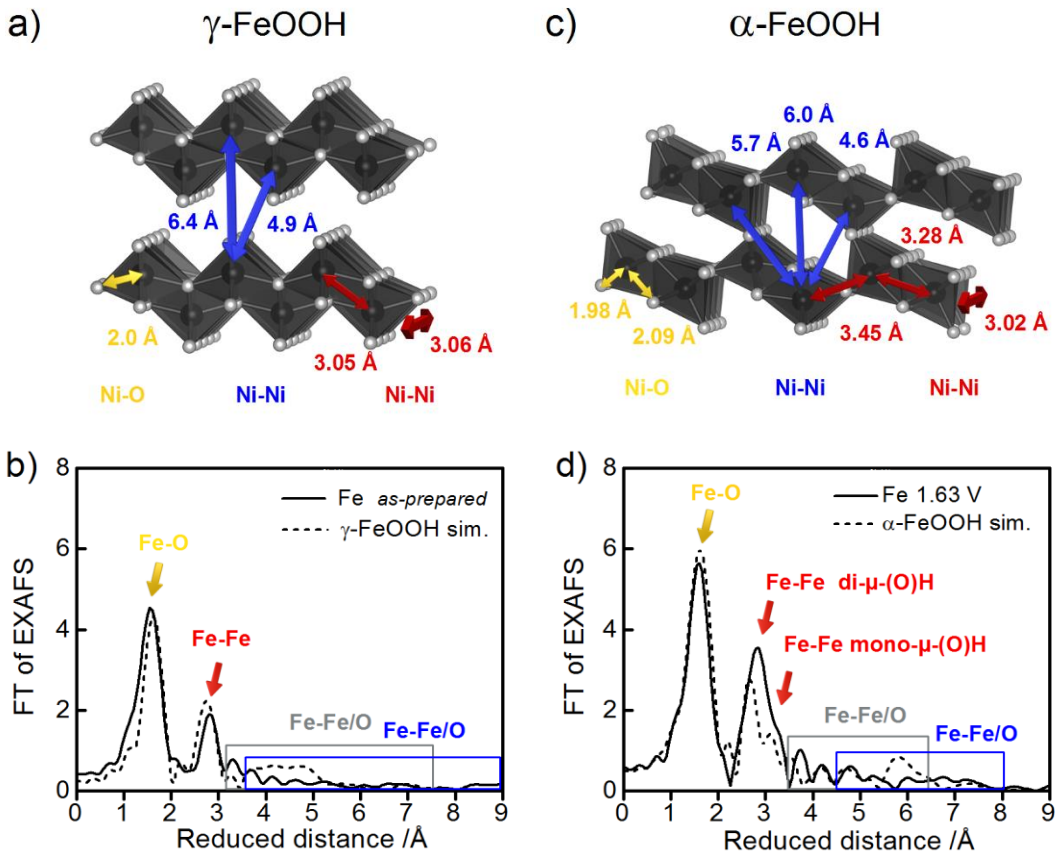

Figure S20. Structural models compared to experimental data at the Fe *K*-edge. **(a)** Structure of γ-FeOOH (cif 9011314) **(b)** FT-EXAFS of the as-prepared Fe catalyst (solid black line) and the simulated spectrum of γ-FeOOH shown in (a) (dashed black line) **(c)** Structure of α-FeOOH (cif 1008766) **(d)** FT-EXAFS of the Fe catalyst at 1.63 V; experimental data (solid black line) and the simulated spectrum of α-FeOOH shown in (c) (dashed black line). The arrows indicate the coordination distances for Fe-O (yellow), Fe-Fe (red), and interlayer distances (blue). The boxes show regions associated with double or multiple scattering. The FT amplitudes of the simulated spectrum of γ/α-FeOOH presented in (b) and (d) have been scaled to fit the experimental.

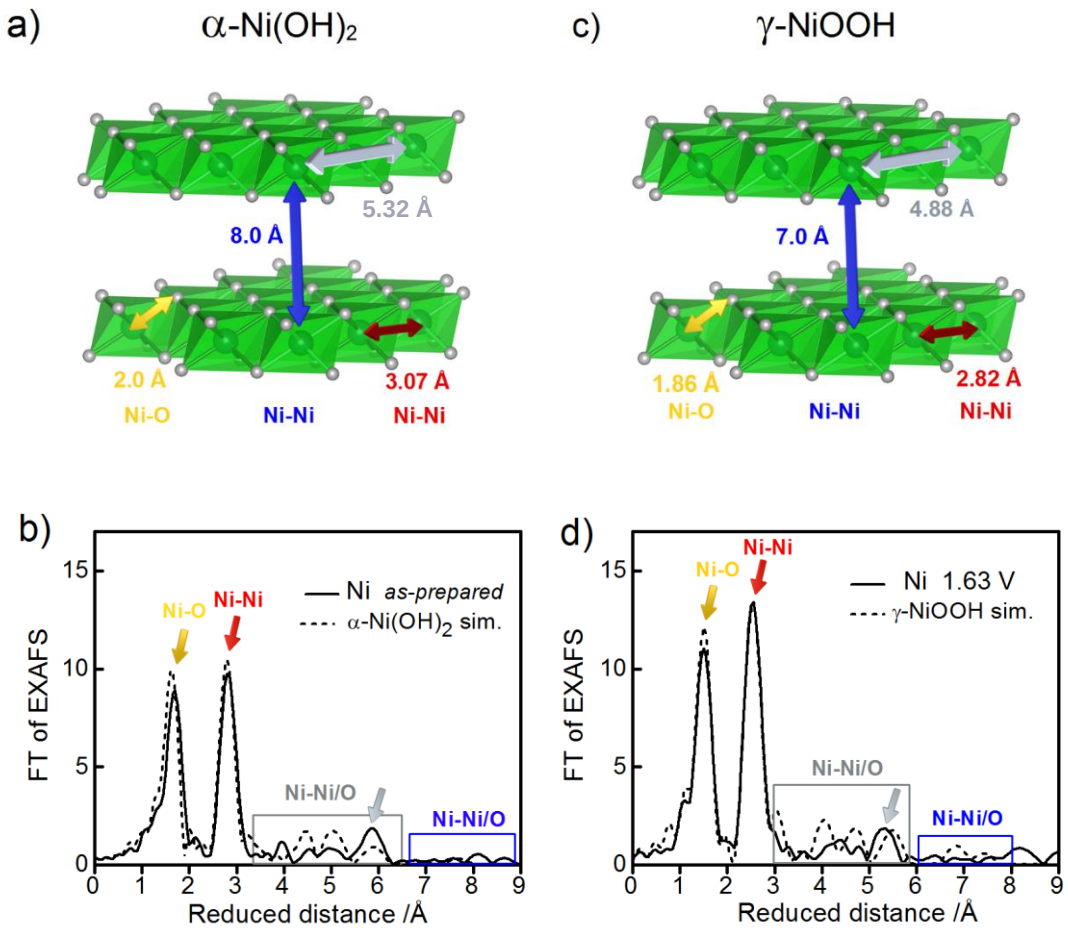

Figure S21. Structural models compared to experimental data at the Ni *K*-edge. (**a)** Structure of α-$Ni(OH)_2$ (cif 9012316) (**b)** FT-EXAFS of the as-prepared Ni catalyst (solid black line) compared to the simulated spectrum of α-$Ni(OH)_2$ shown in (a) (dashed black line). **(c)** The structure γ-NiOOH (cif 9012319) **(d)** FT-EXAFS of the Ni catalyst freeze-quenched at 1.63 V (solid black line) compared to the simulated spectrum of γ-NiOOH shown in (c) (dashed black line). The arrows indicate the coordination distances for Ni-O (yellow), Ni-Ni (red), Ni-Ni double distances (grey), and interlayer distances (blue). The boxes show regions where several distances occur due to presence of double or multiple scattering. The amplitudes of the simulated spectra of α-$Ni(OH)_2$ and γ-NiOOH shown in (b) and (d) have been scaled to fit the experimental data.

S6.3. XAS reference compounds

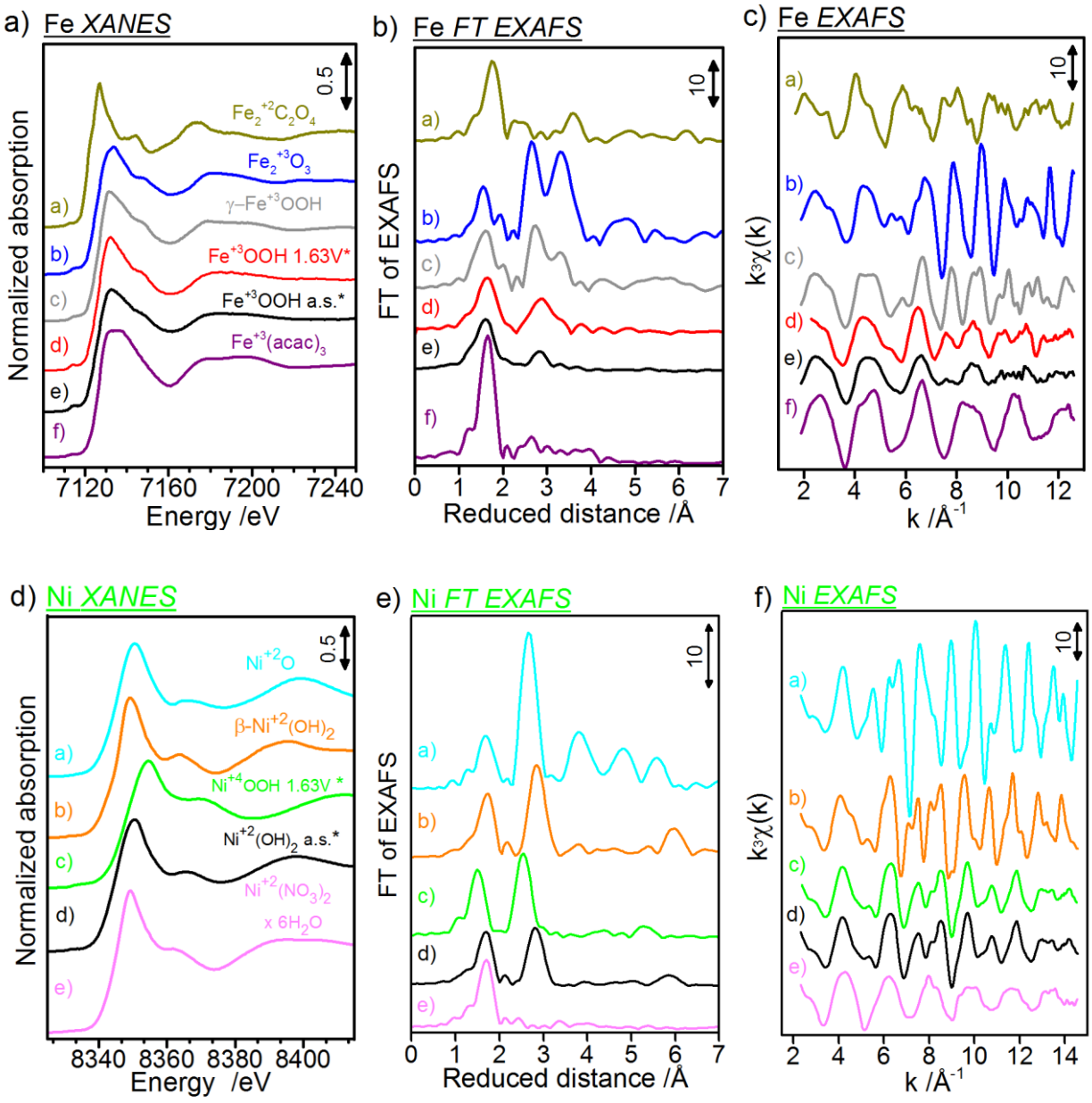

Figure S22. XAS spectra of reference compounds measured at the Ni and Fe *K*-edge. **(a-b)** Ni and Fe XANES. **(c-d)** Ni and Fe k^3 weighted EXAFS oscillations, $k^3\chi(k$. **(d-e)** Fourier transformed FT-EXAFS. Shown Fe compounds; $Fe_2^{(+2)}C_2O_4$ (ALDRICH), $Fe^{2+}{}_3O_3$, γ-$Fe^{+3}OOH$, $Fe^{+3}OOH$ 1.63V (Fe catalyst at 1.63V, * this work, $Fe^{+3}OOH$ a.s. (Fe catalyst a.s.,*this work). Shown compounds are $Ni^{+2}O$ (SIGMA-ALDRICH), β-$Ni^{+2}(OH)_2$ (SIGMA-ALDRICH), $Ni^{+4}OOH$ 1.63V* (Ni catalyst at 1.63V, *this work), and $Ni^{+4}OOH$ (Ni catalyst a.s. *this work), $Ni^{+2}(NO_3)_2$ (ALDRICH).

Table S8. Summary of literature reported EXAFS parameters for the Fe *K*-edge.

Compound	Ox. state	N	R Fe-O (Å)	*K*-edge pos. /eV	Method	Ref
FeC_2O_4	+2	6	2.12	7120.4	EXAFS	[b]
FeO	+2	6	2.120	-	EXAFS	7
α-FeOOH	+3	6	2.020	-	EXAFS	8
α-FeOOH	+3	6	2.000 [a]	-	XRD	9
γ-FeOOH	+3	6	2.000	-	EXAFS	8
γ-FeOOH	+3	6	2.000	-	EXAFS	10
FeOOH (Fhyd 2)	+3.2	6	2.000	-	EXAFS	9
FeOOH (Fhyd 3)	+2.8	6	2.040	-	EXAFS	9
FeOOH (Fhyd 6)	+2.8	6	2.050	-	XRD	9
Fe_2O_3	+3	6	1.98	7124.2	EXAFS	[b]
Fe_2O_3	+3	6	2.045	-	XRD	11
Fe_2O_3	+3	6	2.020 [a]	-	EXAFS	12
Fe_3O_4	+3	5	2.018 [a]	-	EXAFS	12
$Fe(acac)_3$	+3	6	2.0	7125.1	EXAFS	[b]
$SrFeO_3$	+4	-	1.923	-	ND	13
FeOS	+4	-	1.670	-	EXAFS	14

[a] The weighted average of the two given Fe-O shells. [b] Reported EXAFS data was measured in this work

Table S9. Summary of literature reported EXAFS parameters for the Ni *K*-edge

Compound	Ox. state	N	R Ni-O (Å)	*K*-edge position (eV)	Method	Ref
α-$Ni(OH)_2$	+2	6	2.050	-	EXAFS	[15]
α-$Ni(OH)_2$	+2	6	2.050	-	EXAFS	[10]
α-$Ni(OH)_2$	+2	6	2.037	-	EXAFS	[16]
α-$Ni(OH)_2$	+2	6	2.050	-	EXAFS	[17]
α-$Ni(OH)_2$	+2	6	2.040	-	EXAFS	[18]
β-$Ni(OH)_2$	+2	6	2.06	8342.7	EXAFS	[b]
β-$Ni(OH)_2$	+2	6	2.063	-	EXAFS	[16]
β-$Ni(OH)_2$	+2	6	2.070	-	EXAFS	[17]
β-$Ni(OH)_2$	+2	6	2.060	-	EXAFS	[18]
β-$Ni(OH)_2$	+2	6	2.074	-	EXAFS	[19]
$Ni(OH)_2$	+2	6	2.050	8341.7	EXAFS	[20]
$Ni(OH_2)_6$	+2	6	-	8342.9	EXAFS	[21]
NiO	+2	6	2.06	8342.1	EXAFS	[b]
NiO	+2	6	2.090	-	EXAFS	[22]
NiO	+2	6	2.074	-	EXAFS	[16]
NiO	+2	6	2.070	8341.9	EXAFS	[20]
NiO	+2	6	2.070	8342.3	EXAFS	[21]
$Ni(NO_3)_2$	+2	6	2.05	8342.9	EXAFS	[b]
β-NiOOH	+3	6	1.916	-	EXAFS	[19]
β-NiOOH	+3.16	6	1.920	-	EXAFS	[23]
β-NiOOH	+3.26	6	1.922	8343.9	EXAFS	[21]
β-NiOOH	+3	6	1.950		EXAFS	[20]
γ-NiOOH	+3.60	6	1.890	-	EXAFS	[10]
γ-NiOOH	+3.67	6	1.860	-	EXAFS	[17]
γ-NiOOH	+3.67	6	1.888	-	EXAFS	[19]
γ-NiOOH	+3.60	6	1.880	-	EXAFS	[23]
γ-NiOOH	+3.76	6	1.880	8345.0	EXAFS	[21]
$KNiIO_6$	+4	6	1.876	8342.9	EXAFS	[16]
$KNiIO_6$	+4	6	1.870	8345.8	EXAFS	[20]
$KNiIO_6$	+4	6	1.873	-	EXAFS	[24]

[a] The weighted average of the two given Fe-O shells. [b] Reported EXAFS data was measured in this work

References

(1) Batchellor, A. S.; Boettcher, S. W. *ACS Catalysis* **2015**, *5*, 6680.

(2) Smith, R. D. L.; Berlinguette, C. P. *Journal of the American Chemical Society* **2016**, *138*, 1561.

(3) Trotochaud, L.; Young, S. L.; Ranney, J. K.; Boettcher, S. W. *Journal of the American Chemical Society* **2014**, *136*, 6744.

(4) Ankudinov, A. L.; Ravel, B.; Rehr, J. J.; Conradson, S. D. *Physical Review B* **1998**, *58*, 7565.

(5) Rehr, J. J.; Albers, R. C. *Reviews of Modern Physics* **2000**, *72*, 621.

(6) Dau, H.; Liebisch, P.; Haumann, M. *Anal Bioanal Chem* **2003**, *376*, 562.

(7) Thoral, S.; Rose, J.; Garnier, J. M.; Van Geen, A.; Refait, M. P.; Traverse, A.; Fonda, E.; Nahon, D.; Bottero, J. Y. *Environ Sci Technol* **2005**, *39*, 9478.

(8) Suzuki, S.; Suzuki, T.; Kimura, M.; Takagi, Y.; Shinoda, K.; Tohji, K.; Waseda, Y. *Applied Surface Science* **2001**, *169–170*, 109.

(9) Manceau, A.; Schlegel, M. L.; Musso, M.; Sole, V. A.; Gauthier, C.; Petit, P. E.; Trolard, F. *Geochimica et Cosmochimica Acta* **2000**, *64*, 3643.

(10) Friebel, D.; Louie, M. W.; Bajdich, M.; Sanwald, K. E.; Cai, Y.; Wise, A. M.; Cheng, M.-J.; Sokaras, D.; Weng, T.-C.; Alonso-Mori, R.; Davis, R. C.; Bargar, J. R.; Nørskov, J. K.; Nilsson, A.; Bell, A. T. *Journal of the American Chemical Society* **2015**, *137*, 1306.

(11) Fleet, M. *Acta Crystallographica Section B* **1981**, *37*, 917.

(12) Corrias, A.; Ennas, G.; Mountjoy, G.; Paschina, G. *Physical Chemistry Chemical Physics* **2000**, *2*, 1045.

(13) Hodges, J. P.; Short, S.; Jorgensen, J. D.; Xiong, X.; Dabrowski, B.; Mini, S. M.; Kimball, C. W. *Journal of Solid State Chemistry* **2000**, *151*, 190.

(14) Krest, C. M.; Silakov, A.; Rittle, J.; Yosca, T. H.; Onderko, E. L.; Calixto, J. C.; Green, M. T. *Nat Chem* **2015**, *7*, 696.

(15) Balasubramanian, M.; Melendres, C. A.; Mini, S. *The Journal of Physical Chemistry B* **2000**, *104*, 4300.

(16) Mansour, A. N.; Melendres, C. A. *The Journal of Physical Chemistry A* **1998**, *102*, 65.

(17) Capehart, T. W.; Corrigan, D. A.; Conell, R. S.; Pandya, K. I.; Hoffman, R. W. *Applied Physics Letters* **1991**, *58*, 865.

(18) Pandya, K. I.; Ogrady, W. E.; Corrigan, D. A.; McBreen, J.; Hoffman, R. W. *Journal of physical chemistry (1952)* **1990**, *94*, 21.

(19) Morishita, M.; Ochiai, S.; Kakeya, T.; Ozaki, T.; Kawabe, Y.; Watada, M.; Tanase, S.; Sakai, T. *Journal of the Electrochemical Society* **2008**, *155*, 936.

(20) Farley, N. R. S.; Gurman, S. J.; Hillman, A. R. *Electrochimica Acta* **2001**, *46*, 3119.

(21) Risch, M.; Klingan, K.; Heidkamp, J.; Ehrenberg, D.; Chernev, P.; Zaharieva, I.; Dau, H. *Chemical Communications* **2011**, *47*, 11912.

(22) Fominykh, K.; Chernev, P.; Zaharieva, I.; Sicklinger, J.; Stefanic, G.; Döblinger, M.; Müller, A.; Pokharel, A.; Böcklein, S.; Scheu, C.; Bein, T.; Fattakhova-Rohlfing, D. *ACS Nano* **2015**, *9*, 5180.

(23) Bediako, D. K.; Lassalle-Kaiser, B.; Surendranath, Y.; Yano, J.; Yachandra, V. K.; Nocera, D. G. *Journal of the American Chemical Society* **2012**, *134*, 6801.

(24) Currie, D. B.; Levason, W.; Oldroyd, R. D.; Weller, M. T. *Journal of the Chemical Society, Dalton Transactions* **1994**, 1483.

.